Effect of Activated Alloys on Hydrogen Discharge Kinetics of MgH_2 Nanocrystals

Z. Dehouche[1*], H.A. Peretti[2], S. Hamoudi[1], Y. Yoo[3] and K. Belkacemi[1**]

[1]Department of Soil Sciences and Agri-Food Engineering, Université Laval, St-Foy, Quebec, Canada, G1K 7P4;

[2]Centro Atómico Bariloche, 8400 S.C. de Bariloche (RN), Argentina ;

[3]Institute for Chemical Process and Environmental Technology, NRC, Ottawa, ON, Canada, K1A 0R6

[1*] Current address: School of Engineering and Design, Brunel University, Uxbridge, Middlesex UB8 3PH, UK

[**]Corresponding author: Tel: (418) 656 2131 ext: 6511; Fax: (418) 656 3723; E-mail: Khaled.belkacemi@sga.ulaval.ca

Abstract

Activated alloys synthesized by arc-melting were examined as catalysts for improving the hydrogen sorption characteristics of nanostructured magnesium hydride, proposed as a reversible hydrogen storage material. The MgH_2-catalyst absorbing materials were prepared by ball milling of pure MgH_2 with hydrided $Zr_{47}Ni_{53}$, Zr_9Ni_{11}, and other investigated alloys. The nanostructured MgH_2-intermetallic systems were tested at 250°C and catalyst addition of eutectoid $Zr_{47}Ni_{53}$ resulted in the fastest desorption time and highest initial desorption rate. Also, the catalyzed Mg-hydride with activated Zr_9Ni_{11} and Zr_7Ni_{10} phases showed fast desorption kinetics. Moreover, the results demonstrated that the composition of dispersed Zr_xNi_y catalysts has a strong influence on the amount of accumulated hydrogen and desorption rate of Mg-nanocomposite.

Keywords:

Hydrogen storage materials (A); Intermetallics (A); Nanostructures (A); High-energy ball milling (B); X-ray diffraction (C).

1. Introduction

Improving reversible hydrogen sorption rates of solid-state stores at moderate temperature are of great technological importance for the adoption of hydrogen for transportation and stationary applications. Among the different metal hydrides types (Fig. 1) developed previously [1], magnesium-based hydrides are of particular interest for hydrogen storage due to the high energy density they can provide (7.6 H-wt%). From large number of studies available, currently emerges a general perspective that optimum sorption hydrogen storage characteristics may be reached only in catalytically enhanced systems [1-2].

Improved sorption characteristics of nanocrystalline MgH_2 by doping with transition metals and oxides were previously reported. Recent papers by Oelerich et al., Hanada et al. and Skripnyuk et al. [3-5] give an overview of catalyzed MgH_2 nanocomposites prepared by mechanically milling for the hydrogen storage applications. A storage capacity of 6.5wt% after doping MgH_2 with nanosized-Ni in a temperature range of 150-250ºC was reported by Hanada et al. [5]. Moreover, a remarkable improvement in desorption kinetics was also observed by the same group [6] by using 1mol.% Nb_2O_5-doped nanostructured MgH_2 at 160°C under helium flow. More recently, Kojima et al. [7], reported that nano-Ni/Al2O5/C catalysts composite have significant effect in enhancing the sorption kinetics of ball milled MgH2 at 200°C and vacuum condition.

While such catalysts give substantial rise to the sorption rates, further increase in the kinetic and thermodynamic properties of nanostructured Mg-hydride could be possible by using new activated phases of alloys. The aim of this work is to explore the ability of different binary and ternary metal alloys as catalysts to increase the hydrogen sorption properties of nanostructured

magnesium hydride.

2. Experimental details

Synthesis of the nanocomposite materials

The synthesis of the nanocrystalline Mg-based compounds was accomplished by milling a mixture of elemental magnesium hydride (98% pure, from Th. Goldschmidt AG), with intermetallic alloys powders acting as catalysts. The fraction of catalyst added to MgH_2 represents approximately 10 wt.% in each case. The mixtures were sealed in a 30 mL -hardened stainless steel vial set. The vial was vigorously agitated for 20 hours under argon atmosphere. A Spex CertiPrep 8000M mixer (Metuchen, NJ) was used for synthesis of sorption nanocomposites. Details on this nanoscale grinding method were previously described elsewhere [1]. Oxidation and/or hydroxide formation were avoided by storing and handling the samples and starting powders in a glove box filled with pure argon. The alloys were prepared by arc-melting the metallic mixtures in argon atmosphere on a water cooled copper heart. The intermetallic alloys were activated (hydrided) prior to milling by direct reaction with high-pressure hydrogen of 25 atm at 300 °C in the case of Mg_2Ni and at ambient temperature for the other ones.

The other composites were prepared using a similar approach, except for MgH_2-(Zr_7Ni_{10}-AX21), MgH_2-$CMgNi_3$ and MgH_2-$Zr_{47}Ni_{53}$. In the case of MgH_2-(Zr_7Ni_{10}-AX21) 0.2 mol.%, AX21 activated carbon was milled with Zr_7Ni_{10} catalyst, and then the resulting catalyst particles were milled with pure MgH_2 for 20 hours. The super activated carbon used in the experiment is the well-known AX-21 (Anderson Development Co.) exhibiting a BET surface area of *circa* 2800 m^2/g and a total pore volume of 1.1 cm^3/g. To prepare MgH_2-$CMgNi_3$ 2 mol.% nanocomposite,

the ternary compound containing Mg-C-Ni ($MgCNi_3$, non-oxide perovskite) was first synthesised by synergic combination of mechanical alloying and isothermal heating, according to the procedure reported by Ferretti et al. [8].

The chosen composition of the $Zr_{47}Ni_{53}$ alloy (47wt.% Zr, 53wt.% Ni) corresponds to an eutectoid composition solidifying at 1070ºC. The alloy was obtained by arc-melting a pellet containing appropriate amounts of ZrH_2 (-325 mesh, 99% pure) and Ni powder (3 micron, 99.7% pure), previously mixed and compressed at a pressure of 15 tons/cm^2, under vacuum. The resulting alloy button was crushed into pieces before being utilized to prepare the composite. One part of these pieces was used in the as-melted condition, while others were annealed 24 hours at 1000ºC inside an evacuated-quartz capsule. Two samples of composite were obtained: either with as-cast or with annealed $Zr_{47}Ni_{53}$ alloy.

Characterization and cycling

Changes in thermodynamic and kinetic properties of Mg-hydride nanocomposites were determined by carrying out advanced volumetric hydrogen titration and cycling experiments [1]. The microstructure was determined by scanning electron microscopy (SEM) using a field emission scanning electron microscope Hitachi model S4700. The X-ray diffraction analysis was performed on a Rigaku diffractometer with monochromated Co K_α radiation. Specific surface areas of the sample before and after cycling were determined by the Brunauer, Emmett and Teller (BET) technique using nitrogen in a Quantachrome micrometric adsorption analyser at 77 K. Before analyses, heat treatment in a vacuum (10^{-6} atm) at 300°C was applied for several hours.

The samples were characterized and cycled at 250°C and 300°C under ultra high purity hydrogen absorption pressure of 10 atm and a desorption pressure of 0.25 atm. Instantaneous absorption and desorption hydrogen flow rates were measured under the same conditions. The hydrogen sorption rates were determined by measuring directly the rates at which hydrogen is added or extracted to or from the sorption nanocomposites to maintain a constant pressure. The hydrogen sorption rates were monitored by a *Brooks's* mass flow rate controller. Before starting every absorption/desorption experiment, 200 mg-samples were outgassed for at least 30 min at a vacuum pressure of 10^{-6} atm.

3. Results and discussion

Results of the activation of various Zr_xNi_y alloys are presented in Fig. 2. Generally, the alloys formed stable hydrides at ambient temperature. After activation, ZrNi absorbed nearly 2.50 H wt.%, while Zr_7Ni_{10} and Zr_9Ni_{11} absorbed about 1.40 H-wt.%. The activation process metamorphosed alloys into fine powders. This transformation was beneficial since it generated a more homogeneous catalyst particle distribution after milling. Indeed, it was observed that the catalytic enhancements were more important when the hydrogenated catalysts were milled with MgH_2 [1].

Before starting the desorption and PCT experiments, the Mg-based nanocomposite samples were cycled until the desorption rates were stabilized. Dynamic desorption experiments at 250 °C were undertaken on MgH_2-catalyst sorption materials (Fig. 3a, 3b), and the corresponding desorption flow rates were obtained at 250 and 300 °C (Fig. 4a and 4b).

Desorption kinetic properties calculated from measured curves are listed at Table 1. The oscillations observed on the kinetic curves of Fig. 4a were ascribed to the relatively small

difference between desorption plateau pressures and hydrogen pressure in the reactor. Such oscillations were not displayed on the desorption flow rate curves obtained at 300 °C, since the pressure variations in the reactor were negligible in comparison to the driving pressure at the same temperature. It should also be noted that the kinetic measurements at 250 °C showed a better representation of the influence of the various catalysts, since hydrogen diffusivity in the sorption material, which increases with temperature, is by far less important at 250 °C than 300 °C. At high temperatures, high hydrogen diffusivity effectively hides the catalytic effect of the alloys. Considering the time at which the hydrogen desorption flow rates became approximately nil on the 250 °C curves, important variations of this time occured with different catalysts. However, at 300 °C, this time is approximately equal for all catalysts, indicating that dehydrogenation at this temperature does not significantly depend on the intermetallic alloys catalytic properties.

Catalytic addition of $Zr_{47}Ni_{53}$ to MgH_2 resulted in the fastest desorption time and highest initial desorption rate, which are 11 minutes and 0.71 H-wt.%/min, respectively (Fig. 3a). The maximum flow rate of 20.4 cc/min/g measured at 250 °C on MgH_2-$Zr_{47}Ni_{53}$ 10 wt.% was also the highest among all the samples (Fig. 4a). This result constitutes a significant improvement in comparison to that obtained with nanocrystalline MgH_2, which desorbed the hydrogen in about 90 minutes at 300 °C [1]. Annealing the sample increased the desorption time by a small factor, reaching 13 minutes, while desorption rate decreased slightly to 0.66 H-wt.%/min. The maximum flow rate at 250 °C diminished somewhat to 17.8 cc/min/g when MgH_2-$Zr_{47}Ni_{53}$ 10 wt.% was annealed. The second most efficient catalyst of the set studied in this work was Zr_9Ni_{11}.

MgH_2-Zr_9Ni_{11} 0.2 mol.% nanocomposite desorbed hydrogen in approximately 16 minutes at 250

°C, its initial desorption rate was 0.52 H-wt.%/min and its maximum flow rate was approximately 19.0 cc/min/g at 250 °C. The nanocomposite MgH_2- Zr_9Ni_{11} 0.2 mol.% takes 5 minutes more than MgH_2-$Zr_{47}Ni_{53}$ 10 wt.% to desorb hydrogen, but the former can absorb 0.5 H-wt.% more than the latter. The worst discharge time, around 77 minutes, was obtained with MgH_2-Mg_2Ni 2 mol.% nanocomposite. Furthermore, the results show (Fig. 3b) that Zr_7Ni_{10} alloy concentration had a strong effect on the desorption characteristics of the composite. Among all the samples, the highest and lowest desorbed hydrogen amount measured were respectively 6.01 H-wt.% and 4.50 H-wt.%.

Pressure-composition isotherms were also obtained at 250 °C and 300 °C for each of MgH_2 samples added with various catalysts (Fig. 5a and 5b). Table 2 depicts the isothermal sorption properties extracted from the PCT curves as displayed in Fig. 5a and 5b. The intermetallics significantly increased desorption plateau pressure of MgH_2. Since the plateau pressures decreased exponentially with diminishing temperature, lifting desorption plateau pressures are necessary to obtain a material that desorbs hydrogen at lower temperatures. The relatively high plateau pressures at 250 °C and 300°C generated sufficient driving force to allow hydrogen desorption, which represents a major improvement with respect to pure MgH_2.

While higher desorption plateau pressures are linked to faster hydrogen discharge, other factors such as hydrogen diffusivity in the absorbing nanomaterial influence desorption times. Indeed, the MgH_2-Zr_7Ni_{10} 0.2 mol.% and MgH_2-(Zr_9Ni_{11}) 0.2 mol.% nanocomposites have nearly equal desorption plateau pressures at 250 °C, but the former takes two times more to desorb hydrogen than the latter. Moreover, the desorption plateau pressure of MgH_2-Mg_2Ni 2 mol.% is among the highest measured for all the samples, while it desorbs hydrogen completely within the longest period of time. This indicates that the catalysts do not only lift desorption plateau pressures, but

also have a strong effect on the overall hydrogen desorption kinetics of MgH_2 nanocomposites. Mg crystallite sizes were estimated by X-ray diffraction experiments (Table 3). It is clear that the nature of the catalyst milled with MgH_2 had an important influence on Mg grain size. However, it is clearly shown that the kinetic enhancements were not solely due to Mg crystal reduction. Indeed, the smallest estimated nanocrystallite was obtained for MgH_2-ZrNi 1 mol.% nanocomposite, but ZrNi ranks among the alloys providing the least kinetic improvements, proving that the intermetallic compounds themselves have played a truly intrinsic catalytic role in hydrogen desorption. BET specific surface area analyses were undertaken on some of catalyzed MgH_2 samples. MgH_2-Zr_9Ni_{11} 0.2 mol.%, which desorbs hydrogen completely approximately twice as fast as MgH_2 -V 3 at.% - Ti 2 at.%, has a specific surface area of 20.3 m^2/g, while the measured value for MgH2 -V 3 at.% - Ti 2 at.% was 12.3 m^2/g after cycling [9]. Fig. 6 and 7 show the X-ray crystal structure and SEM micrographs analysis carried out on MgH_2-$Zr_{47}Ni_{53}$ nanomaterial before and after cycling. The pattern after 1000 cycles reveals Zirconium peak disappearance; this can be ascribed to Zr nanocrystals amorphization. The micrographs reveal that in the ball-milled state the nanocomposite particles have a dense structure whereas during the hydrogen absorption and desorption cycling the particles became porous with nanopores randomly distributed in the particles (Fig. 7).

Activated carbon was milled with Zr_7Ni_{10} in order to verify if such addition would result in kinetic enhancements. It was believed that carbon would favour a more efficient catalyst particle distribution. Moreover, recent studies have demonstrated that co-milling metal hydrides with carbon improves hydrogen sorption kinetics [10-16], suggesting that carbon plays a catalytic role. Zr_7Ni_{10} was chosen for the experiment, among the Zr_xNi_y catalysts investigated in this work, because this particular composition is easier to activate, thus easier to turn into a fine

powdery form. Unfortunately, AX21 addition had a detrimental effect on the desorption kinetics by raising the discharge time from 34 to 45 minutes and decreasing the discharge rate from to 0.20 to 0.13 H-wt.%/min. Figure 8 shows the X-ray diffraction patterns taken on MgH_2-(Zr_7Ni_{10}-AX21) 0.2 mol.% and MgH_2-Zr_7Ni_{10} 0.2 mol.% after cycling. Mg_2Ni peaks are present in both curves, but the peak intensity at $2\theta = 52.4°$ is much higher in the pattern of MgH_2-(Zr_7Ni_{10}-AX21) 0.2 mol.%. Mg_2Ni peaks are also found in the diffraction patterns of every other MgH_2-Zr_xNi_y catalyst. The other difference between both curves shown in Figure 8, is related to the presence of ZrC peaks in the pattern of MgH_2-(Zr_7Ni_{10}-AX21) 0.2 mol.% suggesting that milling carbon structures with Zr_xNi_y alloys increases the concentration of Mg_2Ni in the sample. It is believed that the observed kinetic slowdown of MgH_2-(Zr_7Ni_{10}-AX21) 0.2 mol.% can be attributed to such a reduction phenomenon. Following milling and cycling, less catalyst particles in Zr_xNi_y form are present in the sample due to the high reactivity of zirconium with carbon, diminishing thus, the catalytic enhancements.

In order to find alternative intermetallic catalyst systems for improving desorption kinetic of nanocrystalline MgH_2, preliminary investigations on the catalysis potential featured by ternary compounds were carried out. With regard to MgH_2-$MgCNi_3$ nanocomposites, the trend of the structural and superconductive parameters of the ternary catalyst compounds versus the rate and amount of the accumulated hydrogen was never investigated. The X-ray diffraction pattern of the milled and heated Mg_2NiH_4 and AX21 mixture is displayed at Figure 9. This pattern confirms the formation of $CMgNi_3$ as well as the presence of traces of Mg_2Ni and graphite. The sorption results show that the catalytic ad-mixing of $CMgNi_3$ enhanced the discharge performance of MgH_2 by a factor of two, in comparison to the results obtained with the Mg_2Ni-doped MgH_2 hydride. Indeed, MgH_2-$CMgNi_3$ nanocomposite desorbed hydrogen with initial flow rate of 0.12

H-Wt.%/min at 250 °C while MgH_2 -Mg_2Ni desorbed hydrogen at lower initial flow rate of 0.05 H-wt%/min.

More experimental analysis using various ternary alloy catalysts were also investigated and presented on Figures 3a, 5a and 5b. The sorption experiments showed that the catalytic behaviours of these alloys and their influence on the dehydrogenation properties of MgH_2 nanocrystals were very different. The $Ti_{0.2}Zr_{0.8}Ni$ alloy revealed to be the most active and induced the lowest discharge capacity.

4. Concluding remarks

- Hydrogen unloading results demonstrate that doping nanostructured Mg-hydride with activated alloys yields increased desorption kinetics and substantial reduction of discharge temperature of MgH_2 nanocrystals.
- Zr_9Ni_{11} and Zr_7Ni_{10} enhance kinetics, but not as much as eutectoid $Zr_{47}Ni_{53}$
- The results also establish that, the stoechiometry of Zr_xNi_y catalysts has a strong influence on desorption kinetic properties. Indeed, MgH_2-Zr_7Ni_{10} 0.2 mol.% desorbs hydrogen in about twice the time taken in the case of MgH_2-Zr_9Ni_{11} 0.2 mol.%.
- MgH_2-$Zr_{47}Ni_{53}$ nanocomposite exhibits improved sorption and microstructure stability during cycling.
- The Zr_7Ni_{10} catalyzed Mg-hydride ground with activated carbon show a reduction in the dehydriding rate, while the $CMgNi_3$ catalyst exhibits increased desorption flow.

Acknowledgements

We want to thank National Research Council Canada for their financial support. We thank also Ms Agnes Lejeune of University of Québec at Trois-Rivières for here help with the SEM analysis.

References

[1] Z. Dehouche, N. Grimard, Nanocomposite Materials for Hydrogen Storage, Chapter on New Nanotechnology Research, Nova Science Publishers 2006, ISBN: 1-60021-2131.

[2] W. Grochala, P. P. Edwards, Chem. Rev. 104 (2004) 1283.

[3] W. Oelerich, T. Klassen, R. Bormann, Advanced Engineering Materials 3 (2001) 487.

[4] V.M. Skripnyuk, E. Rabkin, Y. Estrin and R. Lapovok, Acta Materialia 52 (2004) 405.

[5] N. Hanada, T. Ichikawa, H. Fujii, J. Phys. Chem. B 109 (2005) 7188.

[6] N. Hanada, T. Ichikawa, S. Hino, H. Fujii, J. Alloys. Compd. 420, 46-49 (2006).

[7] Y. Kojima, Y. Kawai, Tetsuya Haga, J. Alloys. Compd. 424, 294-298 (2006)

[8] M. Ferretti, G. Bruzzone, E. Magnone, S. Rubino, J. Mater. Sci. 39 (2004) 5333.

[9] Z. Dehouche, J. Goyette, T. K. Bose, J. Liang, J. Huot, R. Schulz, Journal of Metastable and Nanocrystalline Materials 377 (2001) 77.

[10] C.X. Shang, Z.X. Guo, Journal of Power Sources, 129 (2004) 73.

[11] A. Zaluska, L. Zaluski, J.O. Ström-Olsen, Reversible Hydrogen Storage Composition, Patent Application Publication US 2001/0018939 A1.

[12] S. Bouaricha, J-P Dodelet, D. Guay, J. Huot , R. Schulz, J. Mater. Res. 16 (2001) 2893.

[13] S.D. Toè, S.L. Russo, A. Maddalena, G. Principi, A. Saber, S. Sartori, T. Spataru, Material

Science and Engineering B 108 (2004) 24.

[14] H. Imamura, S. Tabata, N. Shigetomi, Y. Takesue and Y. Sakata, Journal of Alloys and Compounds 330-332 (2002) 579.

[15] Z. Dehouche, L. Lafi, N. Grimard, J. Goyette and R. Chahine, Nanotechnology 16 (2005) 402.

[16] G.P. Meisner, G.G. Tibbetts, F.E. Pinkerton, C.H. Olk and M.P. Balogh, Journal of Alloys and Compounds 337 (2002) 254.

FIGURE CAPTIONS

Fig. 1 Pressure-composition isotherms of various types of metal hydrides [1]

Fig. 2 Activation of Zr_xNi_y catalysts at 23 °C and 25 atm.

Fig. 3a Desorption kinetics of different Mg-nanocomposites at 250°C

Fig. 3b Desorption kinetics of selected Mg-nanocomposites at 250°C

Fig. 4a Dehydriding rates of different Mg-nanocomposites at 250 °C

Fig. 4b Dehydriding rates of different Mg-nanocomposites at 300°C

Fig. 5a Pressure-composition isotherms of different Mg-nanocomposites at 250 °C

Fig. 5b Pressure-composition isotherms of different Mg-nanocomposites at 300°C

Fig. 6 X-ray diffraction patterns performed on MgH_2-$Zr_{47}Ni_{53}$ nanocomposite before and after cycling.

Fig. 7 SEM micrographs taken on MgH_2-$Zr_{47}Ni_{53}$ 10 wt% nanocomposite (a) before and (b) after cycling.

Fig. 8 X-ray patterns taken on MgH_2-(Zr_7Ni_{10}-AX21) 0.2 mol.% and MgH_2-Zr_7Ni_{10} 0.2 mol.% after cycling.

Fig. 9 X-ray patterns taken after milling AX21 and Mg_2NiH_4 and heating the mixture.

TABLE CAPTIONS

Table 1. Desorption kinetic properties of different ball-milled Mg-nanocomposites (initial pressure of 1 psia and initial discharge rates calculated between 0 and 5 minutes).

Table 2. Isothermal sorption properties of various ball-milled Mg-Nanocomposites.

Table 3. Mg crystallite size of the different ball-milled nanomaterials. [†]See [9] for details.

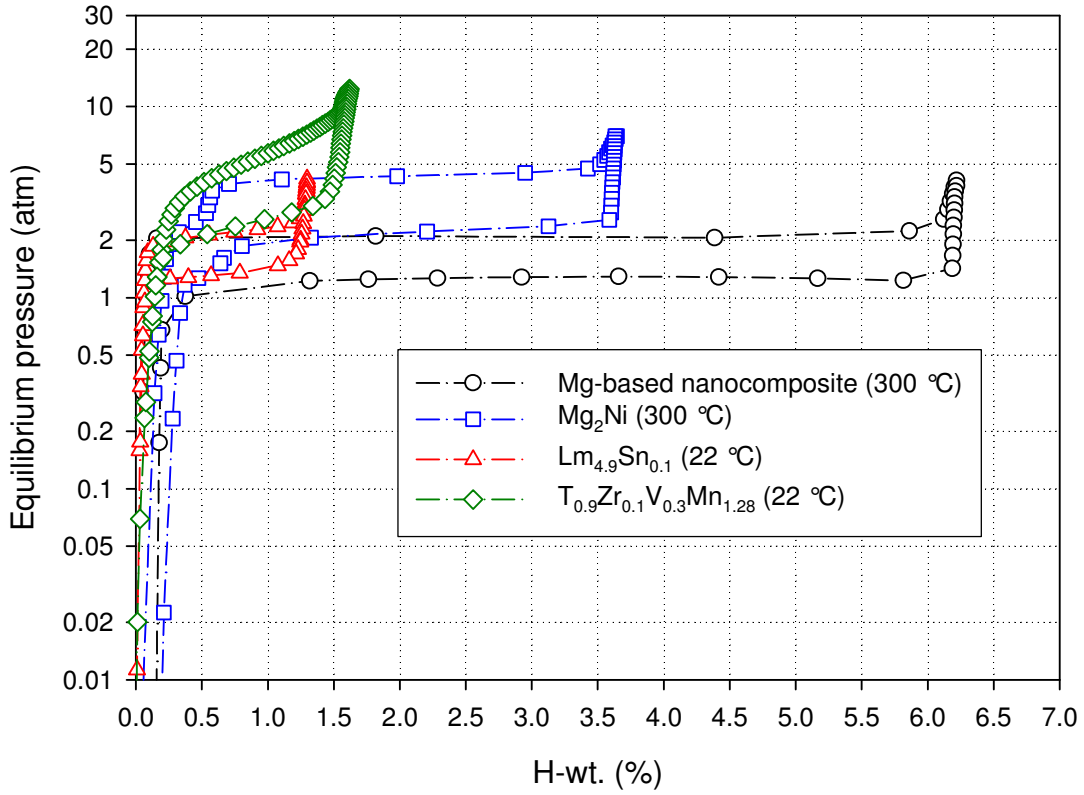
Equilibrium pressure (atm)
30
20
10
5
2
1
0.5
0.2
0.1
0.05
0.02
0.01
0.0
0.5
1.0
1.5
2.0
2.5
3.0
3.5
4.0
4.5
5.0
5.5
6.0
6.5
7.0
H-wt. (%)
Mg-based nanocomposite (300 ℃)
Mg2Ni (300 ℃)
Lm4.9Sn0.1 (22 ℃)
T0.9Zr0.1V0.3Mn1.28 (22 ℃)

Fig. 1

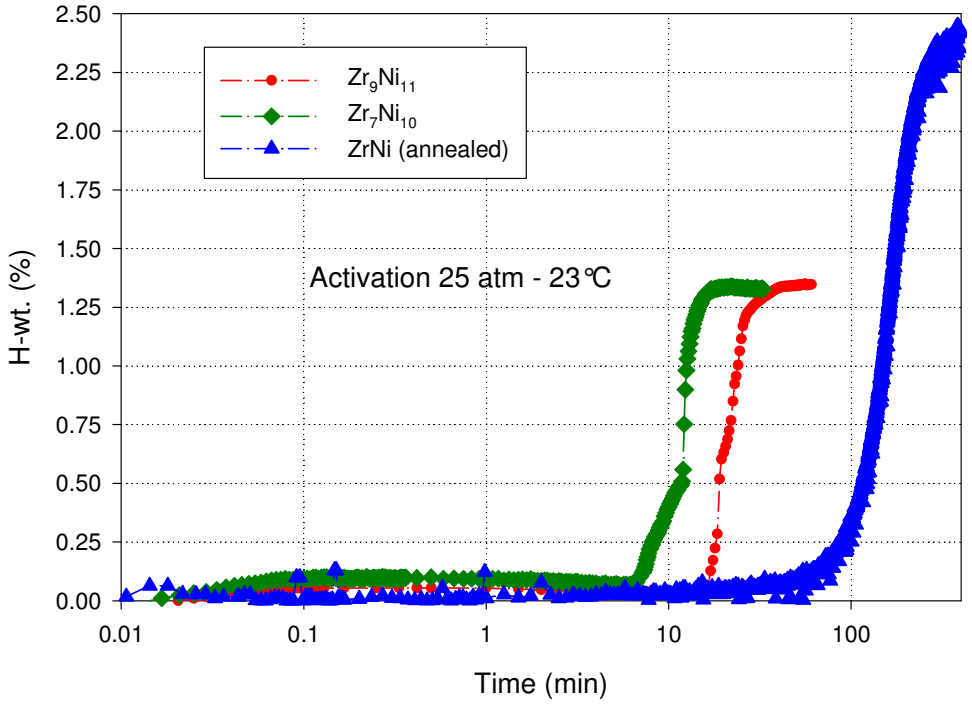
2.50
2.25
2.00
1.75
1.50
1.25
1.00
0.75
0.50
0.25
0.00
H-wt. (%)
0.01
0.1
1
10
100
Time (min)
Zr9Ni11
Zr7Ni10
ZrNi (annealed)
Activation 25 atm - 23℃

Fig. 2

a)

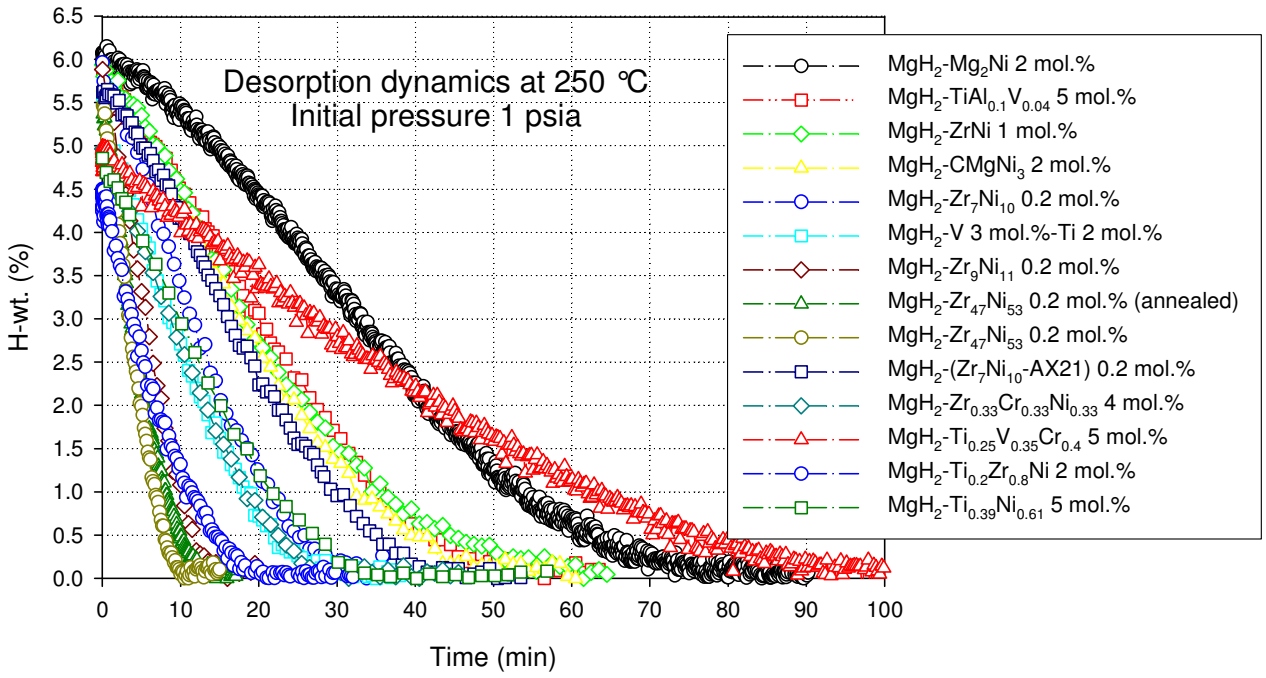
Desorption dynamics at 250 ℃
Initial pressure 1 psia
H-wt. (%)
Time (min)
MgH2-Mg2Ni 2 mol.%
MgH2-TiAl0.1V0.04 5 mol.%
MgH2-ZrNi 1 mol.%
MgH2-CMgNi3 2 mol.%
MgH2-Zr7Ni10 0.2 mol.%
MgH2-V 3 mol.%-Ti 2 mol.%
MgH2-Zr9Ni11 0.2 mol.%
MgH2-Zr47Ni53 0.2 mol.% (annealed)
MgH2-Zr47Ni53 0.2 mol.%
MgH2-(Zr7Ni10-AX21) 0.2 mol.%
MgH2-Zr0.33Cr0.33Ni0.33 4 mol.%
MgH2-Ti0.25V0.35Cr0.4 5 mol.%
MgH2-Ti0.2Zr0.8Ni 2 mol.%
MgH2-Ti0.39Ni0.61 5 mol.%

b)

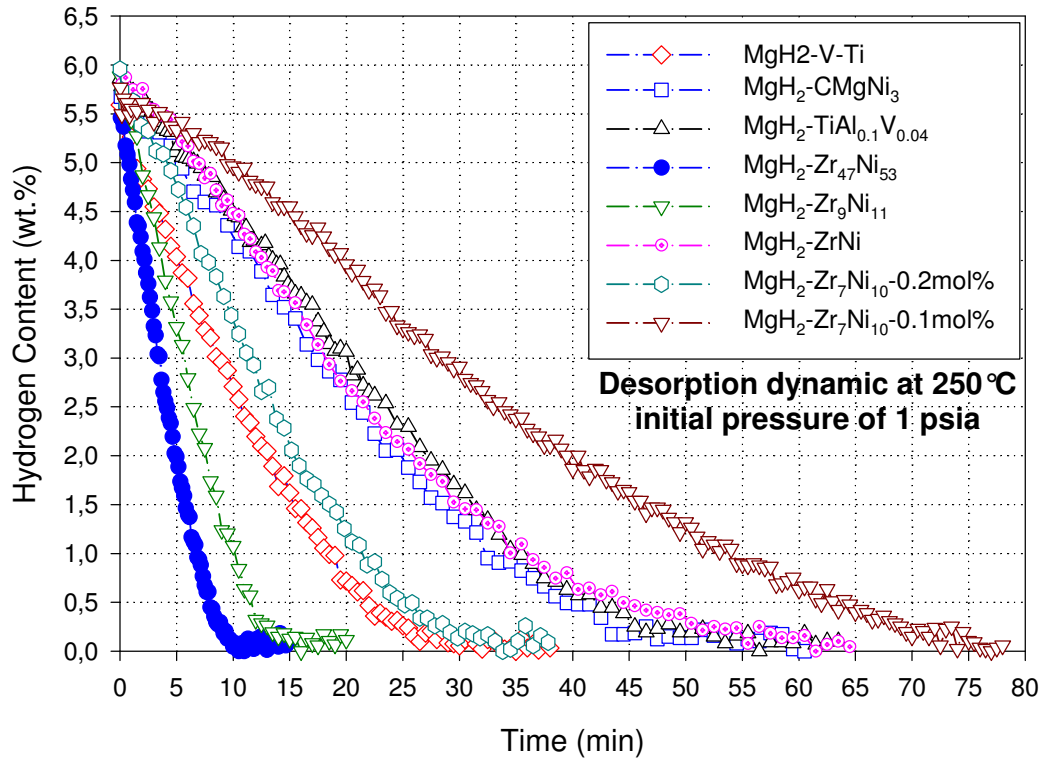
Hydrogen Content (wt.%)
Time (min)
MgH2-V-Ti
MgH2-CMgNi3
MgH2-TiAl0.1V0.04
MgH2-Zr47Ni53
MgH2-Zr9Ni11
MgH2-ZrNi
MgH2-Zr7Ni10-0.2mol%
MgH2-Zr7Ni10-0.1mol%
Desorption dynamic at 250℃
initial pressure of 1 psia

Fig. 3

a)

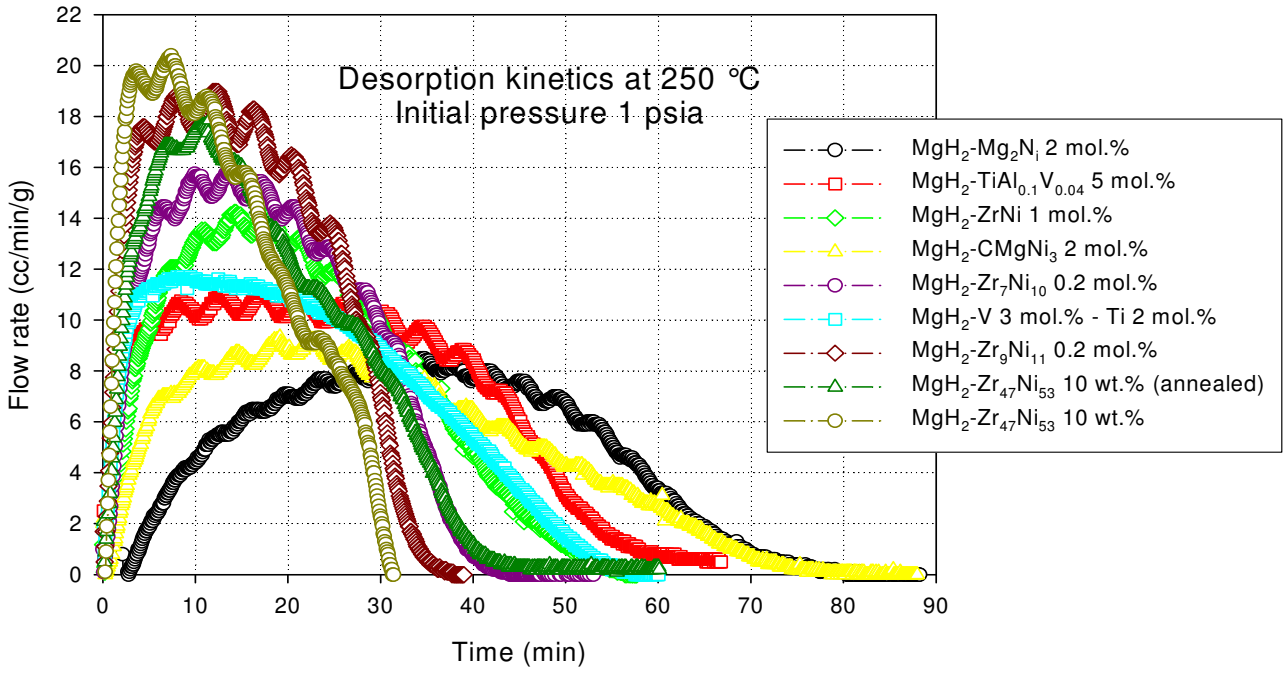
Desorption kinetics at 250 °C
Initial pressure 1 psia
Flow rate (cc/min/g)
Time (min)
MgH2-Mg2Ni 2 mol.%
MgH2-TiAl0.1V0.04 5 mol.%
MgH2-ZrNi 1 mol.%
MgH2-CMgNi3 2 mol.%
MgH2-Zr7Ni10 0.2 mol.%
MgH2-V 3 mol.% - Ti 2 mol.%
MgH2-Zr9Ni11 0.2 mol.%
MgH2-Zr47Ni53 10 wt.% (annealed)
MgH2-Zr47Ni53 10 wt.%

b)

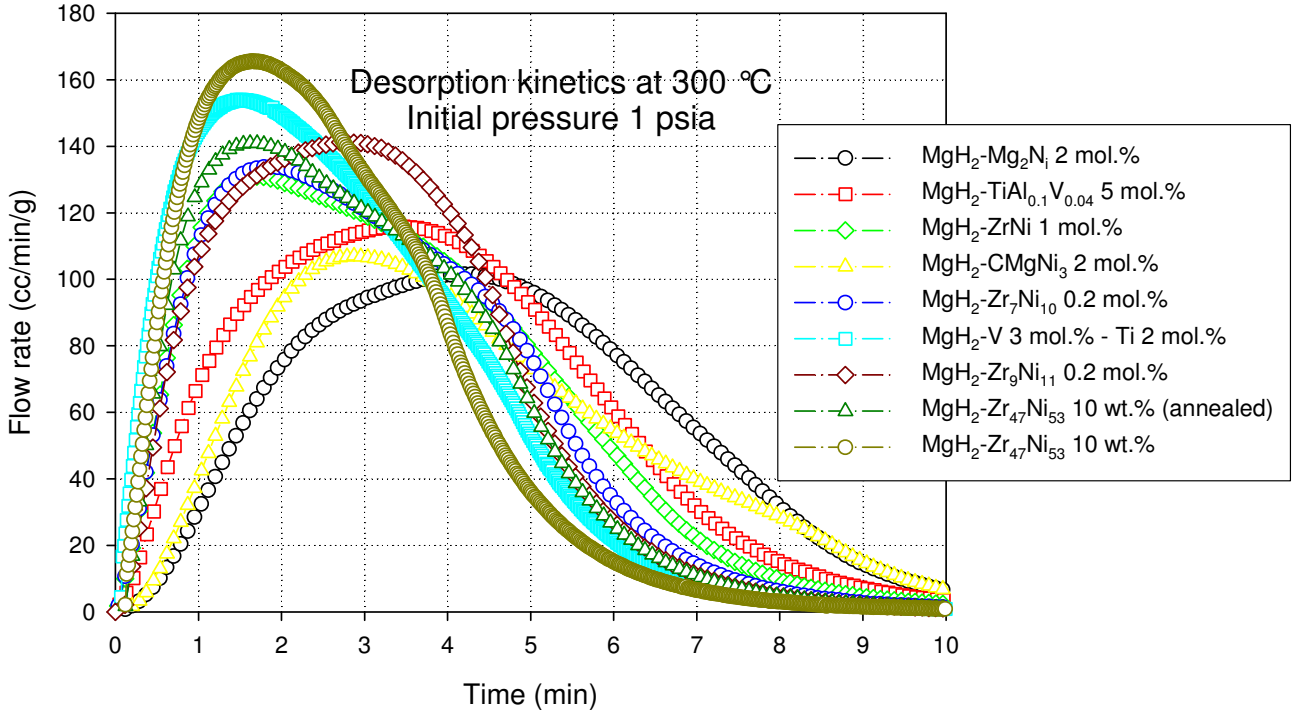
Desorption kinetics at 300 °C
Initial pressure 1 psia
Flow rate (cc/min/g)
Time (min)
MgH2-Mg2Ni 2 mol.%
MgH2-TiAl0.1V0.04 5 mol.%
MgH2-ZrNi 1 mol.%
MgH2-CMgNi3 2 mol.%
MgH2-Zr7Ni10 0.2 mol.%
MgH2-V 3 mol.% - Ti 2 mol.%
MgH2-Zr9Ni11 0.2 mol.%
MgH2-Zr47Ni53 10 wt.% (annealed)
MgH2-Zr47Ni53 10 wt.%

Fig. 4

a)

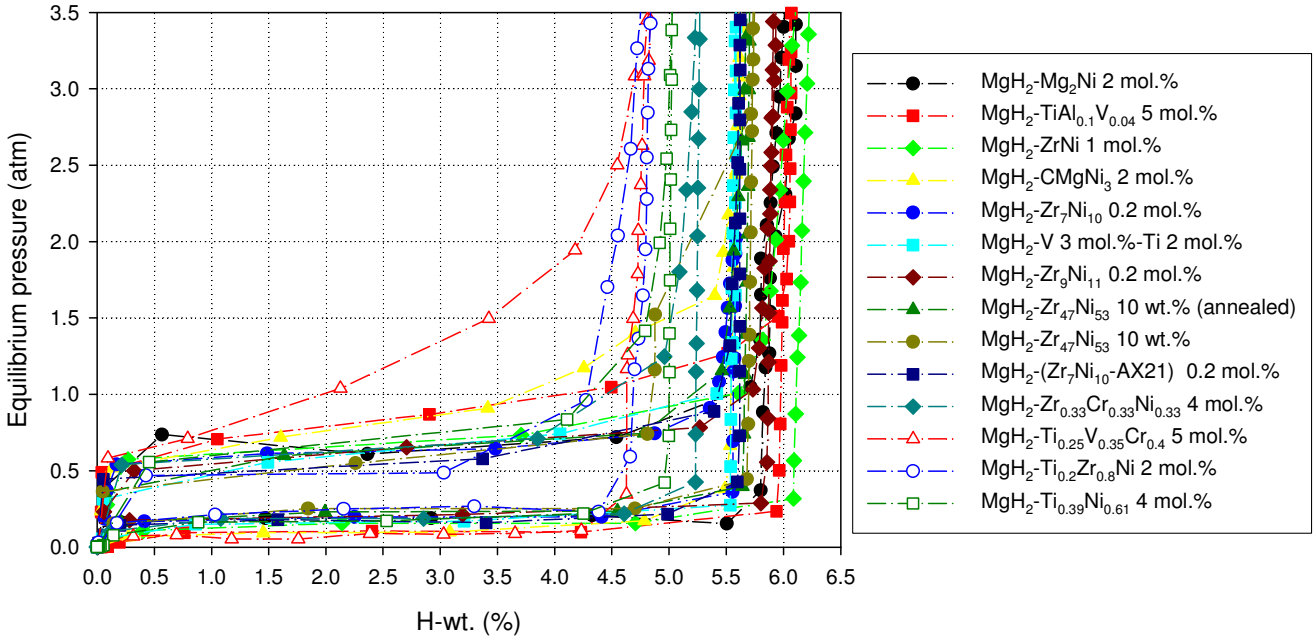
Equilibrium pressure (atm)
H-wt. (%)
0.0
0.5
1.0
1.5
2.0
2.5
3.0
3.5
4.0
4.5
5.0
5.5
6.0
6.5
MgH2-Mg2Ni 2 mol.%
MgH2-TiAl0.1V0.04 5 mol.%
MgH2-ZrNi 1 mol.%
MgH2-CMgNi3 2 mol.%
MgH2-Zr7Ni10 0.2 mol.%
MgH2-V 3 mol.%-Ti 2 mol.%
MgH2-Zr9Ni11 0.2 mol.%
MgH2-Zr47Ni53 10 wt.% (annealed)
MgH2-Zr47Ni53 10 wt.%
MgH2-(Zr7Ni10-AX21) 0.2 mol.%
MgH2-Zr0.33Cr0.33Ni0.33 4 mol.%
MgH2-Ti0.25V0.35Cr0.4 5 mol.%
MgH2-Ti0.2Zr0.8Ni 2 mol.%
MgH2-Ti0.39Ni0.61 4 mol.%

b)

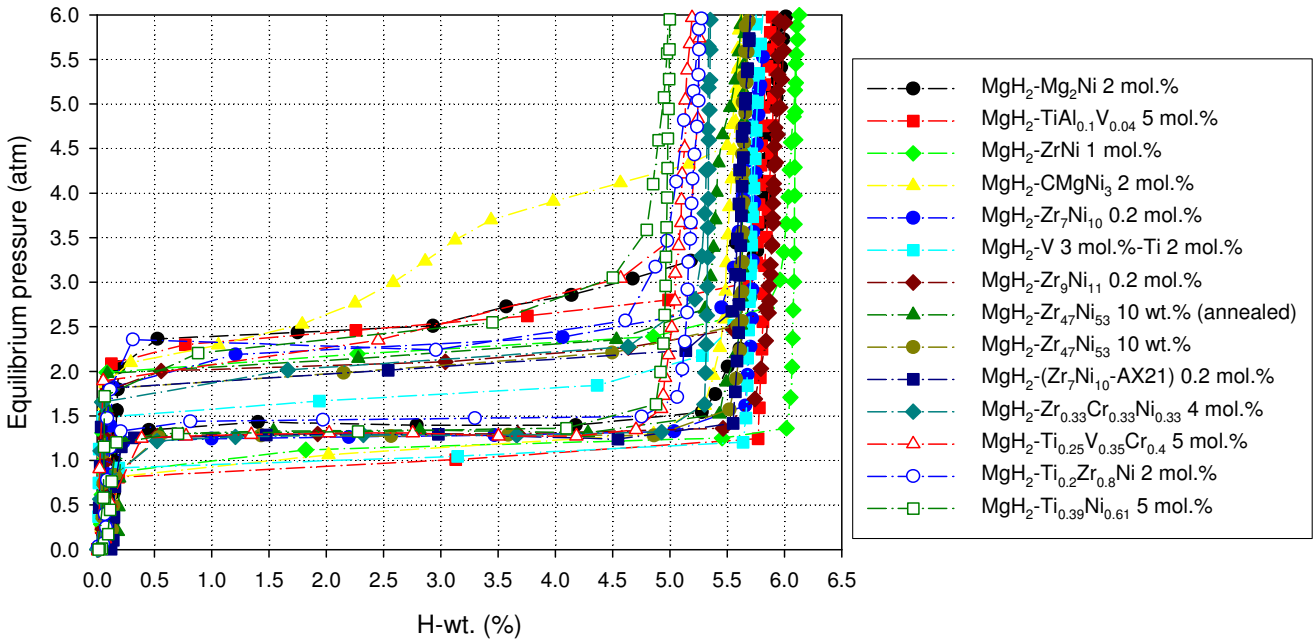
Equilibrium pressure (atm)
H-wt. (%)
0.0
0.5
1.0
1.5
2.0
2.5
3.0
3.5
4.0
4.5
5.0
5.5
6.0
6.5
MgH2-Mg2Ni 2 mol.%
MgH2-TiAl0.1V0.04 5 mol.%
MgH2-ZrNi 1 mol.%
MgH2-CMgNi3 2 mol.%
MgH2-Zr7Ni10 0.2 mol.%
MgH2-V 3 mol.%-Ti 2 mol.%
MgH2-Zr9Ni11 0.2 mol.%
MgH2-Zr47Ni53 10 wt.% (annealed)
MgH2-Zr47Ni53 10 wt.%
MgH2-(Zr7Ni10-AX21) 0.2 mol.%
MgH2-Zr0.33Cr0.33Ni0.33 4 mol.%
MgH2-Ti0.25V0.35Cr0.4 5 mol.%
MgH2-Ti0.2Zr0.8Ni 2 mol.%
MgH2-Ti0.39Ni0.61 5 mol.%

Fig. 5

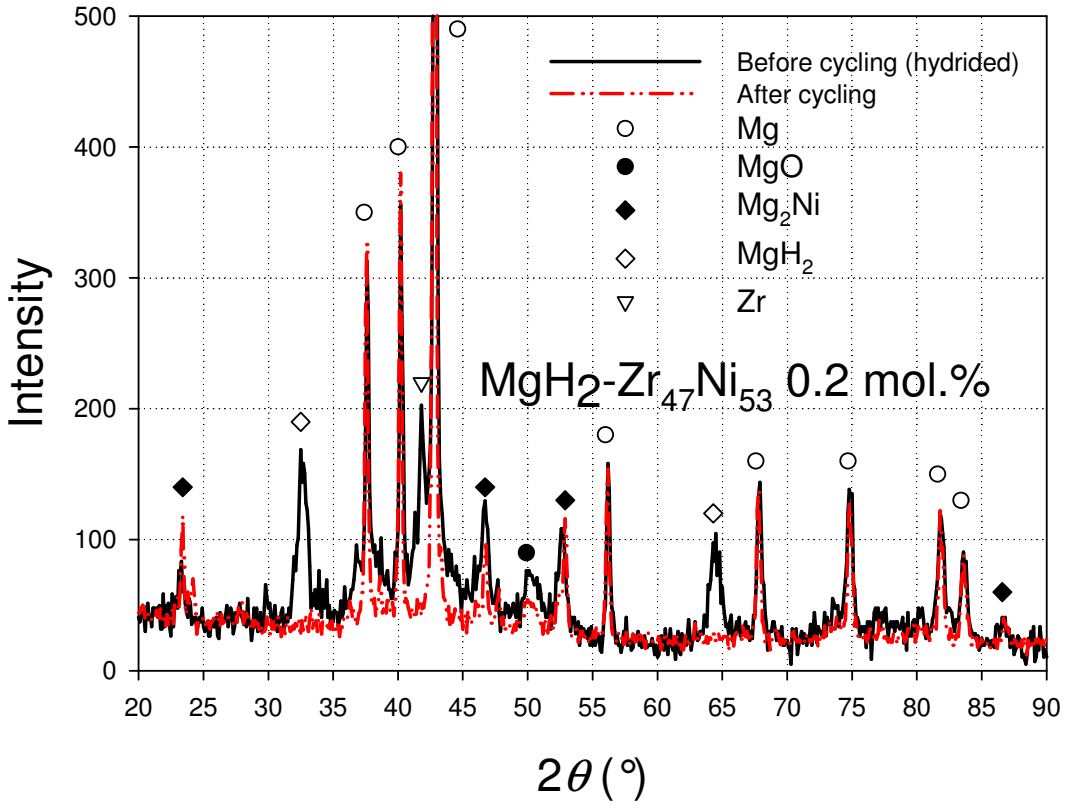
Intensity
2θ (°)
Before cycling (hydrided)
After cycling
Mg
MgO
Mg2Ni
MgH2
Zr
MgH2-Zr47Ni53 0.2 mol.%

Fig. 6

a)

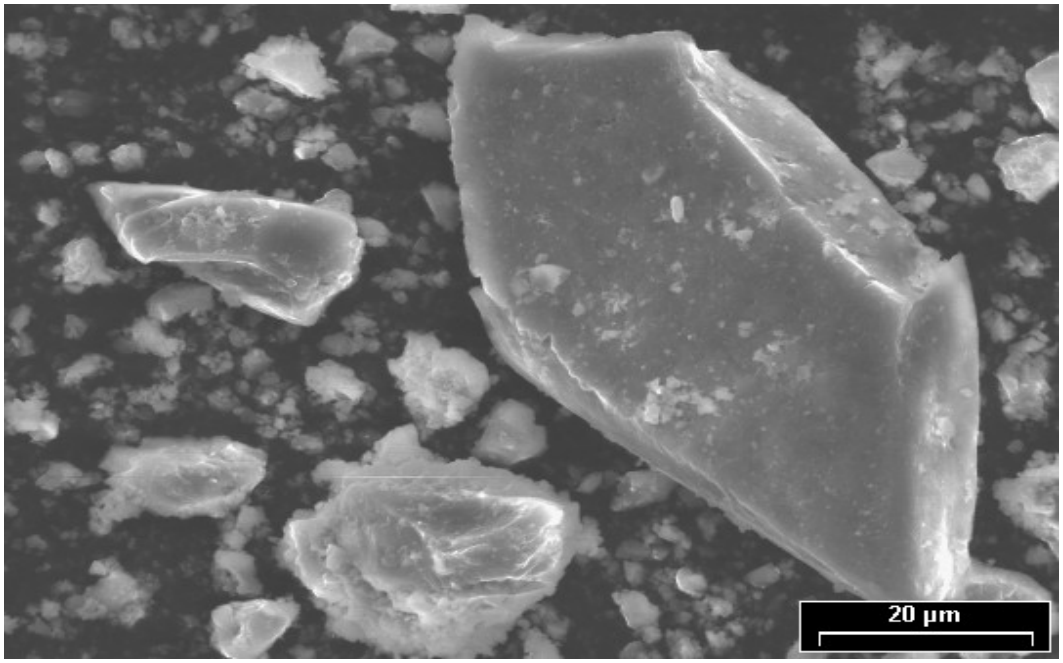

b)

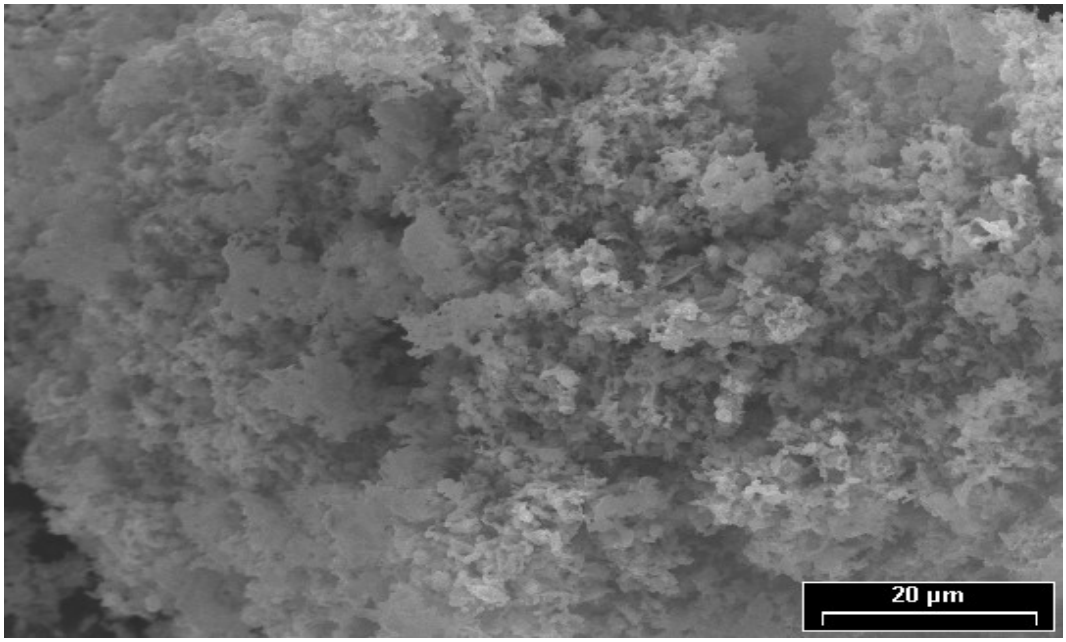

Fig. 7

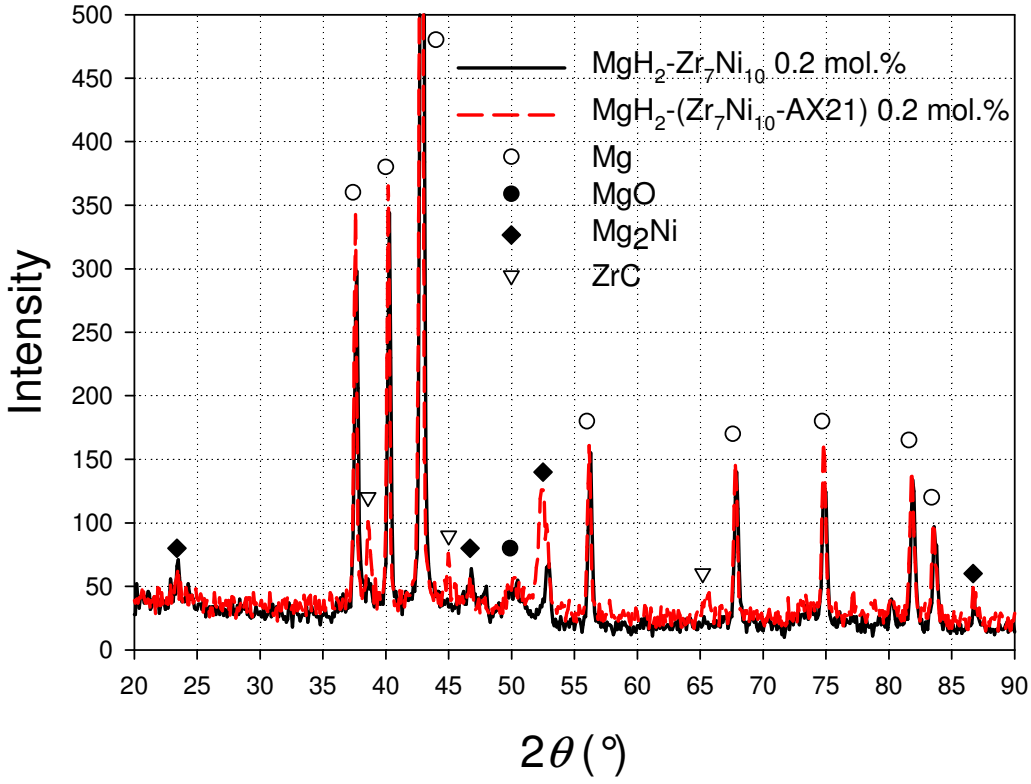
Intensity
2θ (°)
MgH2-Zr7Ni10 0.2 mol.%
MgH2-(Zr7Ni10-AX21) 0.2 mol.%
Mg
MgO
Mg2Ni
ZrC
0
50
100
150
200
250
300
350
400
450
500
20
25
30
35
40
45
50
55
60
65
70
75
80
85
90

Fig. 8

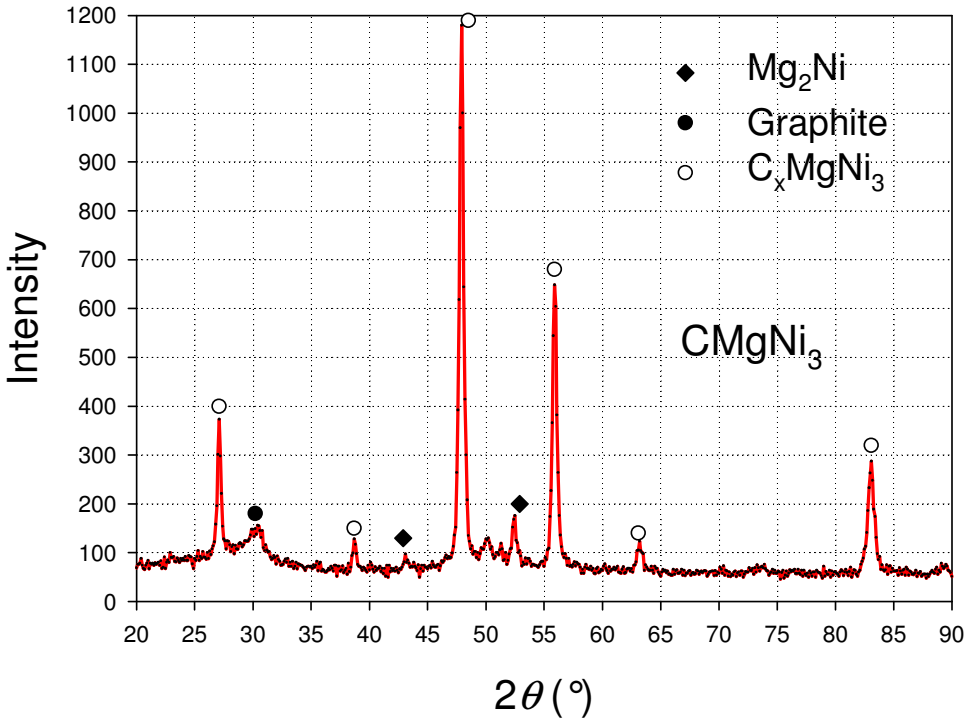

Fig. 9

Table 1

Sample	Initial discharge rate at 250 °C (H-wt. %/min)	Discharge capacity at 250°C (H-wt. %)	Discharge time at 250 °C (min)	Peak flow rate at 250 °C (cc/min/g)	Peak flow rate at 300 °C (cc/min/g)
MgH_2-Mg_2Ni 2 mol.%	0.05	6.01	77	8.5	101.5
MgH_2-$TiAl_{0.1}V_{0.04}$ 5 mol.%	0.13	5.77	54	11.1	115.9
MgH_2-ZrNi 1 mol.%	0.12	5.90	56	14.2	130.9
MgH_2-$CMgNi_3$ 2 mol.%	0.12	5.68	55	9.3	107.0
MgH_2-Zr_7Ni_{10} 0.2 mol.%	0.20	5.91	34	15.7	133.4
MgH_2 –V 3 at.% - Ti 2 at.%	0.31	5.59	32	11.7	153.9
MgH_2-Zr_9Ni_{11} 0.2 mol.%	0.52	5.88	16	19.0	141.2
MgH_2-$Zr_{47}Ni_{53}$ 10 wt.% (annealed)	0.66	5.37	13	17.8	140.9
MgH_2-$Zr_{47}Ni_{53}$ 10 wt.%	0.71	5.42	11	20.4	165.6
MgH_2-(Zr_7Ni_{10}-AX21) 0.2 mol.%	0.13	5.64	45	N/A	N/A
MgH_2-$Zr_{0.33}Cr_{0.33}Ni_{0.33}$ 4 mol.%	0.22	4.96	32	N/A	N/A
MgH_2-$Ti_{0.2}Zr_{0.8}Ni$ 2 mol.%	0.35	4.50	20	N/A	N/A
MgH_2-$Ti_{0.39}Ni_{0.61}$ 5 mol.%	0.19	4.86	35	N/A	N/A

Table 2

Temperature (ºC)	Absorption plateau pressure (atm)	Desorption plateau pressure (atm)	Maximum H. wt (%)	Absorption plateau slope (d ln(P)/ d H/M)	Desorption plateau slope (d ln(P)/ d H/M)	Hysteresis (ln (P_{abs}/P_{des}))
MgH_2-Mg_2Ni 2 mol.%						
250	0.65	0.19	6.21	0.97	0.67	1.22
300	2.53	1.39	6.08	0.67	0.12	0.60
MgH_2-$TiAl_{0.1}V_{0.04}$ 5 mol.%						
250	0.88	0.10	6.09	2.50	0.29	2.15
300	2.54	1.00	6.00	1.03	1.61	0.93
MgH_2-ZrNi 1 mol.%						
250	0.70	0.16	6.34	1.56	1.92	1.50
300	2.25	1.16	6.14	0.73	0.67	0.66
MgH_2-$CMgNi_3$ 2 mol.%						
250	0.87	0.10	5.69	1.93	1.85	2.18
300	3.36	1.14	5.64	1.47	0.88	1.08
MgH_2-Zr_7Ni_{10} 0.2 mol%						
250	0.64	0.20	5.59	1.2	0.85	1.17
300	2.31	1.28	5.81	0.63	0.33	0.59
MgH_2 - V 3 at.% - Ti 2 at.%						
250	0.67	0.17	5.60	2.48	1.17	1.38
300	1.74	1.04	5.88	0.91	1.00	0.52
MgH_2-Zr_9Ni_{11} 0.2 mol.%						
250	0.67	0.21	5.95	1.88	1.86	1.16
300	2.10	1.30	6.03	0.63	0.27	0.48
MgH_2-$Zr_{47}Ni_{53}$ 10 wt.% (annealed)						
250	0.66	0.23	5.75	1.03	0.14	1.05
300	2.21	1.34	5.65	0.62	0.04	0.50
MgH_2-$Zr_{47}Ni_{53}$ 10 wt.%						
250	0.60	0.25	5.80	2.20	1.64	0.87
300	2.06	1.28	5.74	0.68	0.05	0.48
MgH_2-(Zr_7Ni_{10}-AX21) 0.2 mol.%						
250	0.54	0.17	5.64	1.65	0.76	1.16
300	2.01	1.29	5.72	0.91	0.26	0.44
MgH_2-$Zr_{0.33}Cr_{0.33}Ni_{0.33}$ 4 mol.%						
250	0.65	0.19	5.31	1.65	0.97	1.24
300	2.09	1.29	5.36	0.89	0.38	0.49
MgH_2-$Ti_{0.2}Zr_{0.8}Ni$ 2 mol.%						
250	0.48	0.25	4.96	0.31	1.95	0.64
300	2.26	1.46	5.34	1.44	0.19	0.44
MgH_2-$Ti_{0.39}Ni_{0.61}$ 5 mol.%						
250	0.71	0.17	5.08	2.42	1.95	1.42
300	2.41	1.32	5.00	1.23	0.30	0.60

Table 3

Nanocomposite	Mg crystallite size (nm)
MgH_2-Mg_2Ni 2 mol.%	52
MgH_2-$TiAl_{0.1}V_{0.04}$ 5 mol.%	52
MgH_2-ZrNi 1 mol.%	37
MgH_2-$CMgNi_3$ 2 mol.%	49
MgH_2-Zr_7Ni_{10} 0.2 mol.%	38
MgH_2 – V 3 at.% - Ti 2 at.%	54[†]
MgH_2-Zr_9Ni_{11} 0.2 mol.%	43
MgH_2-$Zr_{47}Ni_{53}$ 10 wt.% (annealed)	40
MgH_2-$Zr_{47}Ni_{53}$ 10 wt.% (uncycled)	45
MgH_2-$Zr_{47}Ni_{53}$ 10 wt.%	44
MgH_2-(Zr_7Ni_{10}-AX21) 0.2 mol.%	46
MgH_2-$Zr_{0.33}Cr_{0.33}Ni_{0.33}$ 4 mol.%	42